Supplementary Information

Enabling dendrite-free and high-rate lithium anode with a self-standing anionic-MOF separator

Chengjie Wang[a], Zhendong Hao[b], Yating Hu[a], Yue Wu[a], Jingbing Liu[a], Yuhong Jin[a], Hao Wang[a], Qianqian Zhang[a]**

[a] Key Laboratory for New Functional Materials of Ministry of Education, Faculty of Materials and Manufacturing, Beijing University of Technology, Beijing 100124, P. R. China.

[b] School of Materials Science and Engineering, Nanjing Institute of Technology, Nanjing 211167, China

* Corresponding author. E-mail: liujingbing@bjut.edu.cn; zhangqianqian@bjut.edu.cn

Contents of Supporting Information

1. Theoretical calculations

Based on Nernst-Planck (PNP) equation, the ions concentration distribution was simulated by the modules of "Electrostatics" and "Transport of Diluted Species" in COMSOL Multiphysics 5.6 software, which equations are as follows[1]:

$$J_i = -D(\nabla c_i + \frac{z_i F c_i}{RT}\nabla\phi) \quad \text{S3}$$

$$\nabla^2\phi = -\frac{F}{\varepsilon}\sum z_i c_i \quad \text{S4}$$

$$\nabla \cdot J_i = 0 \quad \text{S5}$$

where J_i, D, z_i, c_i, and ϕ were the ionic flux, the diffusion coefficient of the species, the charge number, the concentration, and the electrical potential, respectively. ε is the dielectric constant of the electrolyte solution. F, R, and T are Faraday constant, universal gas constant, and the absolute temperature, respectively. In 1D single nanochannel model, the electrolyte in the two reservoirs was set as 1 mM KCl aqueous solution. By measuring the UIO-66-SO_3Li in the zeta potential (ξ) of the concentration of KCl aqueous solution to estimate the surface charge density (σ_0), which the equation of calculation is as follows[2,3]:

$$\sigma_0 = \frac{\varepsilon_0 \varepsilon_r \xi}{\lambda_D} \quad \text{S6}$$

Where ε_0 is the dielectric constant of the membrane under vacuum, ε_r is the dielectric constant in the film in aqueous solution, and λ_D is the debye length which was calculated according to the following equation [4]:

$$\lambda = \sqrt{\frac{\varepsilon\varepsilon_0 k_B T}{2n_{bulk} z^2 e^2}} \quad \text{S7}$$

Where the ε and ε_0 are the dielectric constants of the solvent and vacuum, respectively. k_B is the Boltzmann constant, T is the absolute temperature, and n_{bulk} is the concentration of the bulk solution. z is the valence of the ion. e is the charge of the electron. The boundary conditions of

the calculation model are as follows:

$$\vec{n} \cdot \nabla\varphi = -\frac{\sigma_0}{\varepsilon} \quad \text{S8}$$

$$\vec{n} \cdot J_i = 0 \quad \text{S9}$$

where $\vec{n}$ represented the unit normal vector, and σ_0 was the surface charge.

2. SEM of synthesized UIO-66-SO_3Li

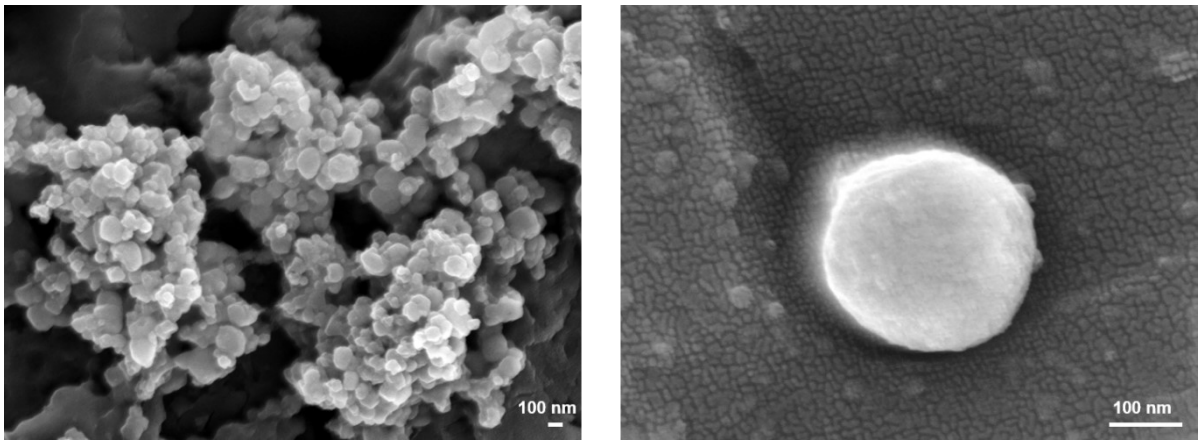

Fig. S1 SEM of synthesized UIO-66-SO_3Li.

3. Cross-sectional SEM images of AMS with different MOF content

As shown in Fig S2, the separator is relatively uniform and flat, which the thickness of AMS with different MOF content (m_{Mof} / m_{Mof} + m_{pvdf}) is a) 4.7 μm, b) 7.9 μm, c) 8.7 μm and d) 9.5 μm, respectively, which m_{Mof} and m_{pvdf} represents the mass of MOF and Polyvinylidene fluoride (PVDF), respectively.

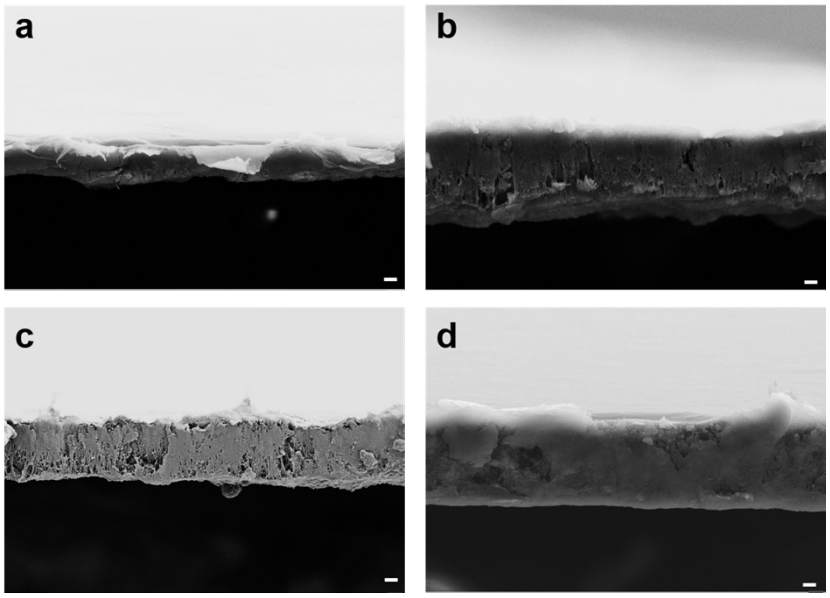

Fig. S2 Cross-sectional SEM images of AMS with different MOF content. a) AMS-40% b) AMS-50% c) AMS-60% d) AMS-70%. Scale bars: 2 μm.

4. Top-view SEM image of the AMS with a higher magnification.

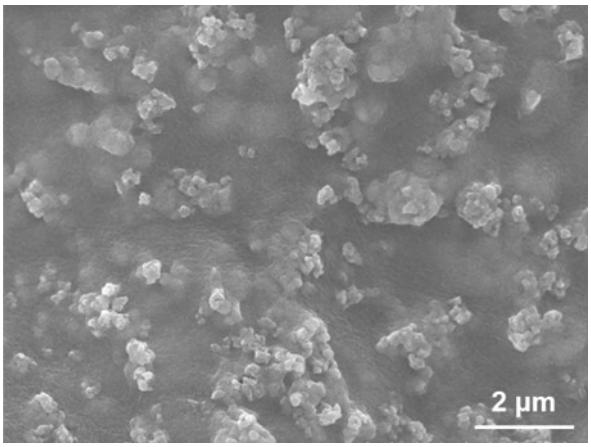

Fig. S3 Top-view SEM image of the AMS with a higher magnification.

5. Bend test of AMS

As shown in Fig. S4, AMS can still be restored after being folded 180 ° along two diagonal lines, and the separator will not break, and the surface separator has a good flexibility.

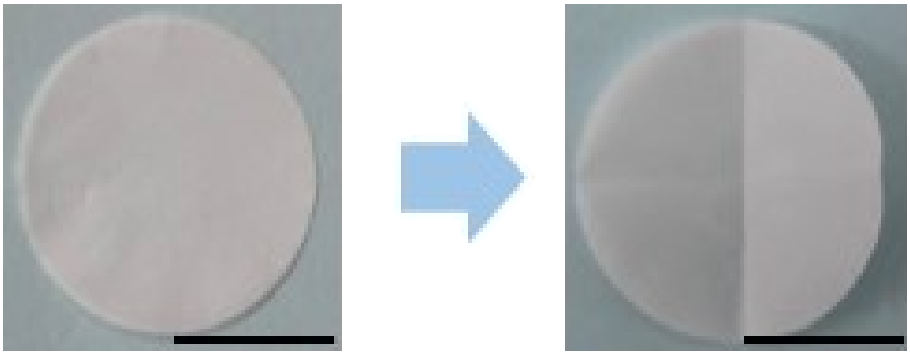

Fig. S4 AMS fold the before and after picture in half diagonally. Scale bars: 1 cm.

6. Electrolyte wettability of CPS

As shown in Fig. S5, the wettability of cps to the commercial electrolyte is poor, and the electrolyte contact Angle is 53.7 °, much higher than the AMS electrolyte contact Angle of 10.0 °. The contact time between lithium hexafluoride electrolyte and CPS is 0.5 s.

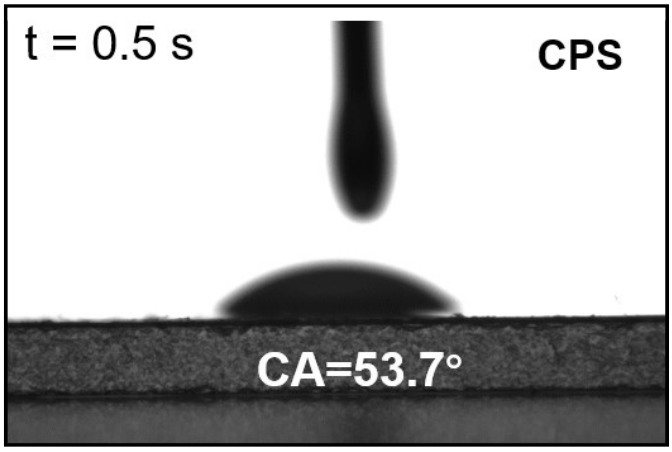

Fig. S5 The surface electrolyte contact angles of CPS.

7. Electrolyte absorption and porosity tests for AMS and CPS

The porosity of the separator and the absorption rate of the electrolyte are important performance indexes of the separator itself. The porosity of the separator was measured by n-butanol immersion method and calculated by the following equation S1:

$$Porosity = (W_2\text{-}W_1) / (\rho \times V) \times 100\% \quad \text{S1}$$

which W_2 and W_1 are the weights of the n-butanol-soaked separator and dry separator, respectively. ρ is the density of the n-butanol and V is the volume of the separator. The porosity of AMS is 54%, which is higher than that of CPS (39%). The electrolyte absorption capacity was tested by soaking the separator in the electrolyte at room temperature for specific intervals. Gently wipe any excess electrolytes on the separator with a filter paper. The electrolyte absorption capacity was calculated by the following equation S2:

$$Electrolyte\ uptake = (W_1\text{-}W_0) / S \times 100\% \quad \text{S2}$$

which W_1 and W_0 are the weights of the separators before and after soaking in the electrolyte, respectively. S is the surface area of the separator. The electrolyte uptake of AMS separator is higher, about 316%, which is 1.6 times higher than that of CPS separator (195%). The high porosity and electrolyte absorption rate of AMS are due to the high specific surface area and excellent affinity for the electrolyte of MOF.

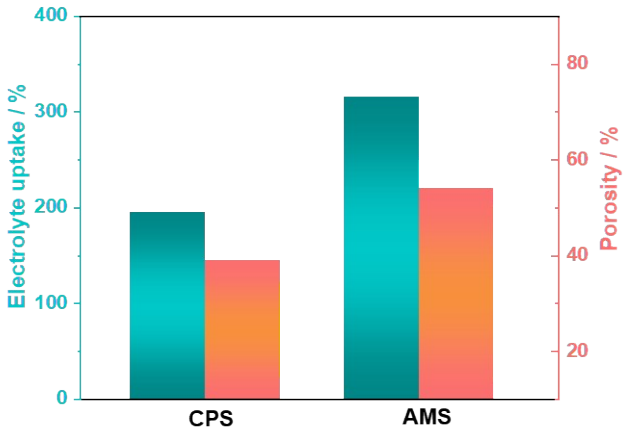

Fig. S6 Electrolyte absorption and porosity tests for AMS and CPS.

8. XRD of UiO-66-SO_3H

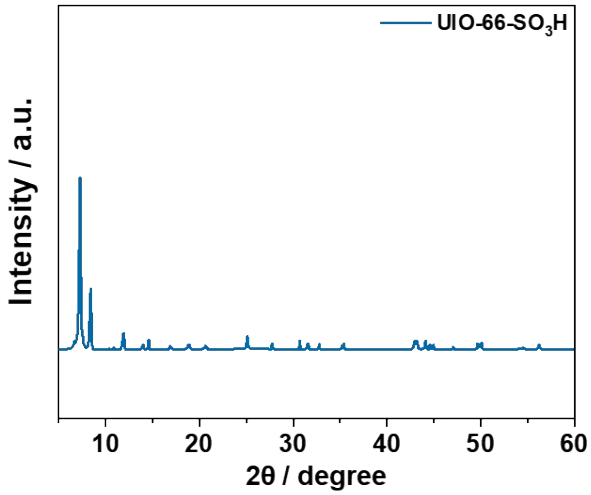

Fig. S7 XRD pattern of UiO-66-SO_3H.

9. Nanopore structure of UIO-66-SO_3Li

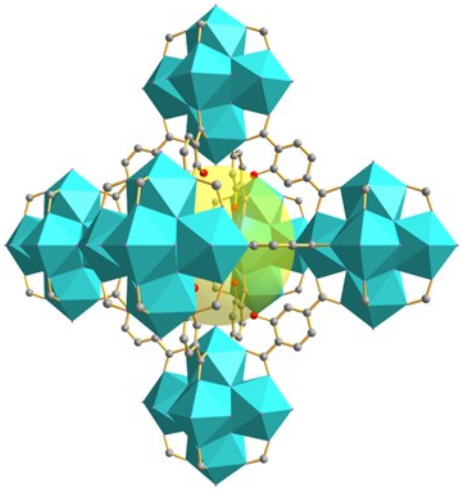

Fig. S8 Nanopore structure of UIO-66-SO_3Li.

10. Nitrogen adsorption and desorption curves of UIO-66-SO_3H

N_2 adsorption and desorption were performed to study the microstructure of MOF. Prior to measurement, the sample was active and degassed at 120 °C for 10 h to remove organic molecules contained in the nanochannel. As shown in Fig S9, the Brunauer–Emmett–Teller (BET) surface area of UIO-66-SO_3H is 438.3 $m^2 g^{-1}$, which was consistent with that reported in the literature[5].

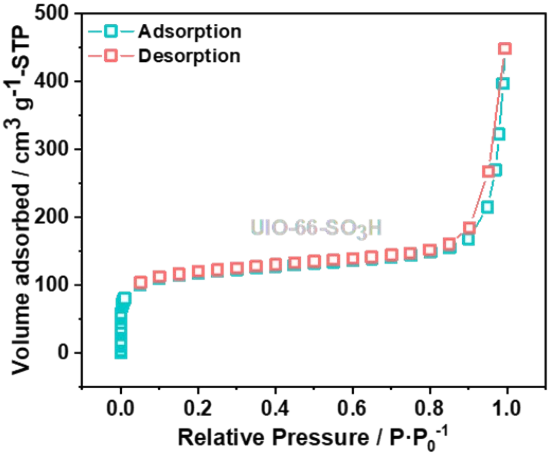

Fig. S9 Nitrogen adsorption–desorption isotherms of UIO-66-SO_3H.

11. FT-IR spectrum of AMS

As illustrated in Fig. S10. the Fourier transform infrared spectroscopy (FT-IR) spectra of AMS reveal the recombination between the PVDF and MOF particles, which confirmed the successful preparation of the separator. The peaks at 637 cm^{-1} and 1587、1401 (O-C-O) / 1170 cm^{-1} (S=O)[6] are ascribed to the metal clusters (Zr-O)[7] and the ligands (BDC-SO_3^-) in the MOF particles, respectively. In addition, the H-F[8] vibration peak originated from PVDF exists at 1076 cm^{-1}.

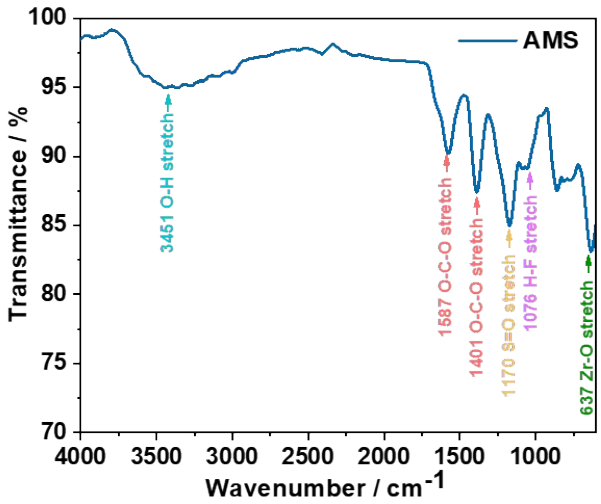

Fig. S10 Fourier transform infrared spectroscopy (FT-IR) spectra of AMS.

12. TGA and DTG curves of CPS

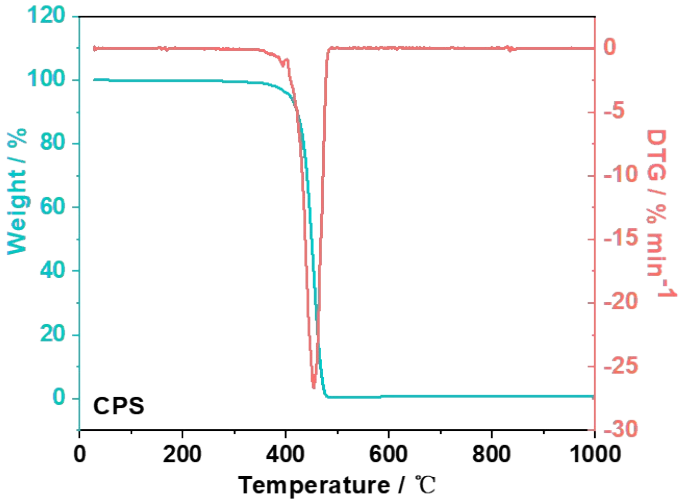

Fig. S11 TGA and DTG curves of the CPS.

13. The hot-treatment pictures of AMS and CPS under different temperatures

To avoid the risk of thermal runaway, the separator also should have good thermal stability. The CPS appeared slightly carbonized at 180 °C, while the CPS had completely softened and curled. In addition, the AMS does not appear obvious crimping at 200 °C, which confirms its better thermal stability.

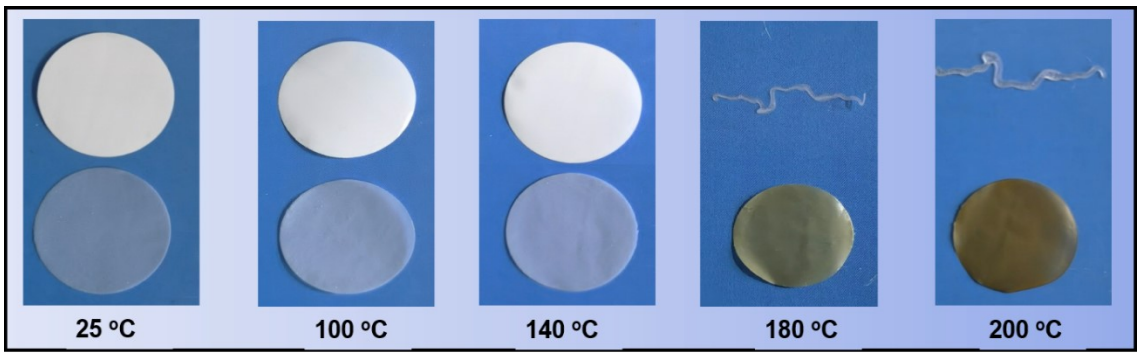

Fig. S12 The hot-treatment pictures of AMS and CPS under different temperatures.

14. Surface water contact angles of AMS and CPS

The surface water contact angles of AMS and CPS were measured. As shown in Fig. S13, the surface water contact angles of AMS and CPS were 68.8 ° and 126.5 °.

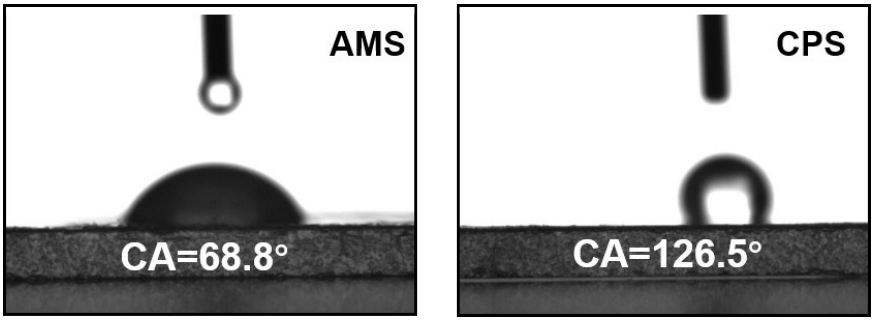

Fig. S13 Surface water contact angles of AMS and CPS.

15. Ion transport regulation of commercial polypropylene separator

As shown in Fig. S14a, although the ion current-voltage (I-V) curve of CPS at different concentrations has linear ohmic characteristics, the transmembrane ion conductance is very low. In addition, ionic conductance is also proportional to the concentration[9] (Fig. S14b). The net 1current of the CPS was much small at the salt concentration gradients (C_{high} / C_{low} = 10000), it shows no cation selectivity (Fig. S14c).

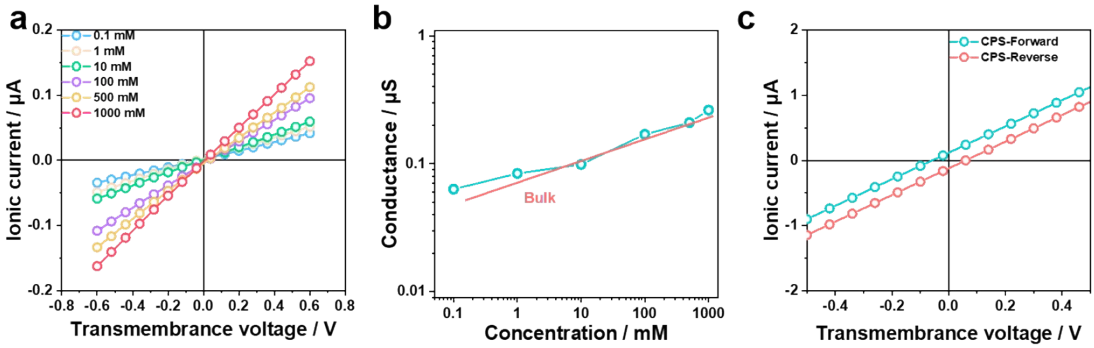

Fig. S14 Ion transport regulation of commercial polypropylene separator.

16. The 1D single nanochannel model for AMS and CPS

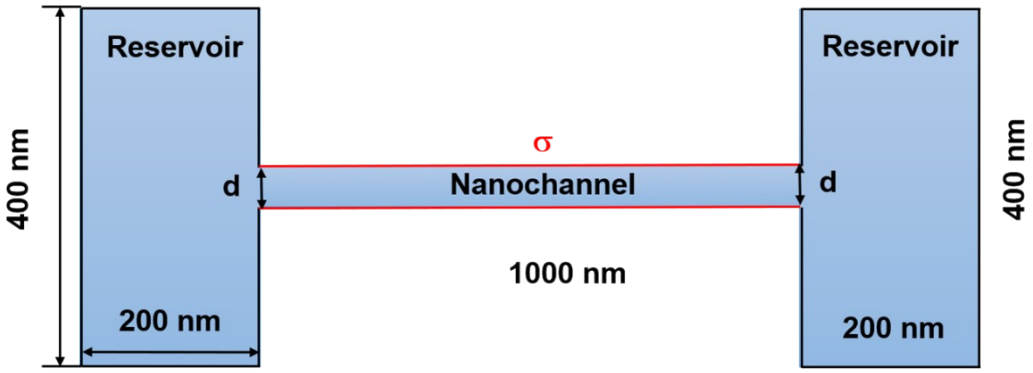

Fig. S15 The 1D single nanochannel model for AMS and CPS.

17. The K^+ and Cl^- concentration profiles of the cps under different potential

As shown in Fig. S16 because CPS has no cation selectivity, the concentration of cationic ions in the channel is basically the same and very low, although there is a certain deviation from the applied voltage.

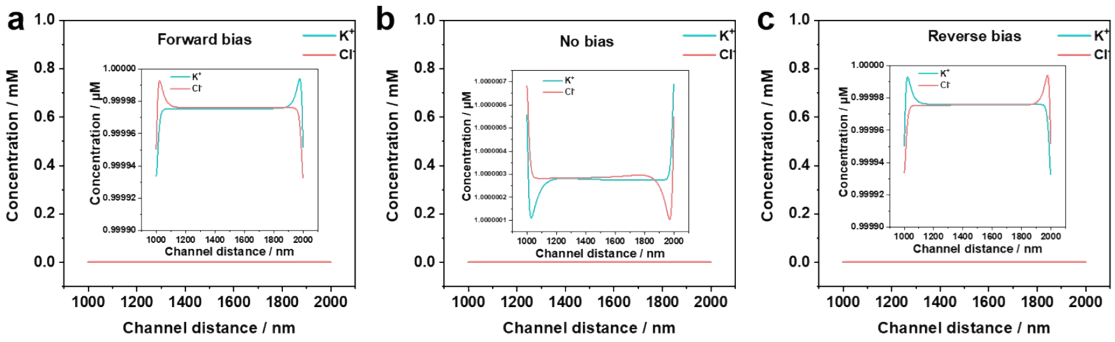

Fig. S16 The K^+ and Cl^- concentration profiles of the cps under a) forward bias (+1 V), b) no bias (0 V), and c) reverse bias (-1 V) based on theoretical simulation.

18. The t_{Li}^+ of AMS with different contents of MOF

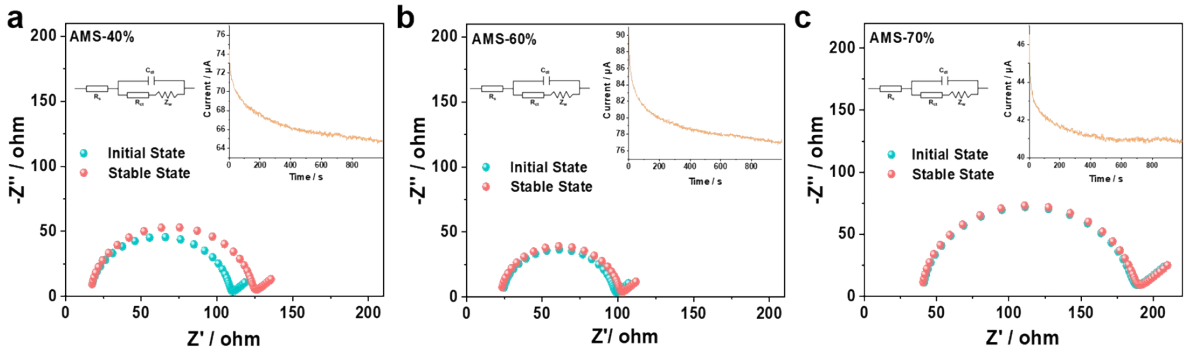

Fig. S17 The t_{Li}^+ of AMS with different contents of MOF

19. Cyclic voltammetry curves of a lithium symmetric coin cells with AMS and CPS

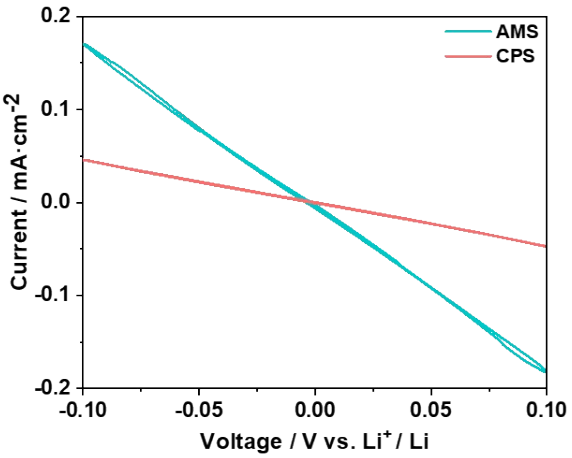

Fig. S18 Cyclic voltammetry curves of a lithium symmetric coin cells with AMS and CPS.

20. Zr 3d XPS spectra of AMS before and after cycling

As shown in the Fig. S19, the two characteristic peaks at 181.0 eV and 183.4 eV in Zr 3d spectrum could be assigned to the hex nuclear Zr_6-octahedron (Zr^{4+}) are interconnected by monosodium 2-Sulfoterephthalate, which was ascribed to the formation of Zr $3d_{5/2}$ and Zr $3d_{3/2}$, respectively.

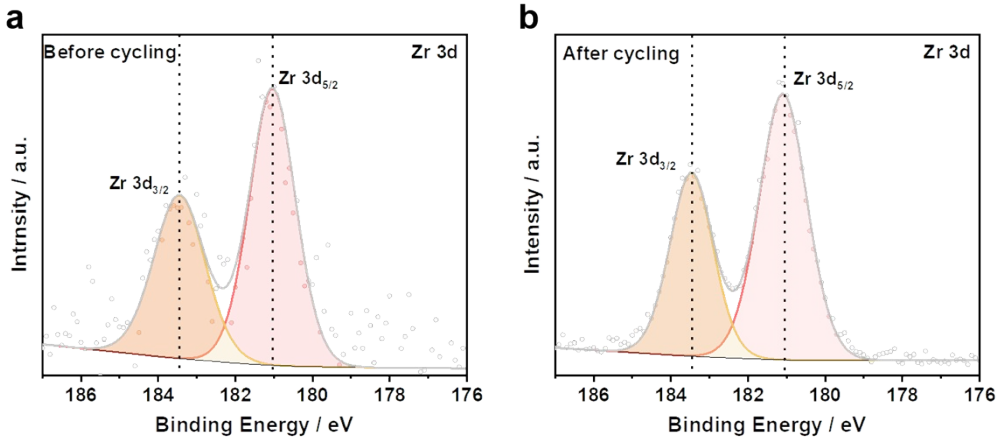

Fig. S19 Zr 3d XPS spectra of lithium symmetric cell with AMS before cycle (a) and after (b) cycling 1000 times

21. Digital and SEM images of free lithium metal anodes

Fresh lithium foil has metallic luster and smooth surface.

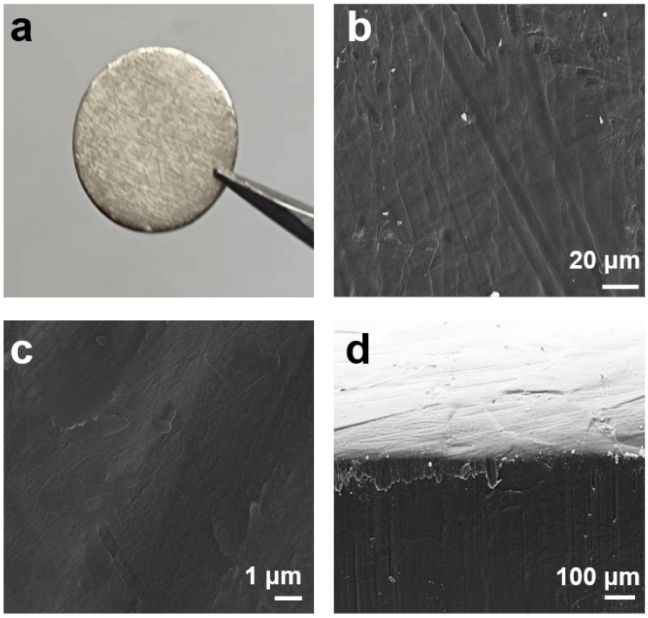

Fig. S20 Digital and SEM images of free lithium metal anodes. a) Digital image, b, c) Top-view SEM images and d) Cross-sectional SEM images of lithium metal anodes.

22. F 1s XPS spectra of the lithium metal cycled with AMS and CPS

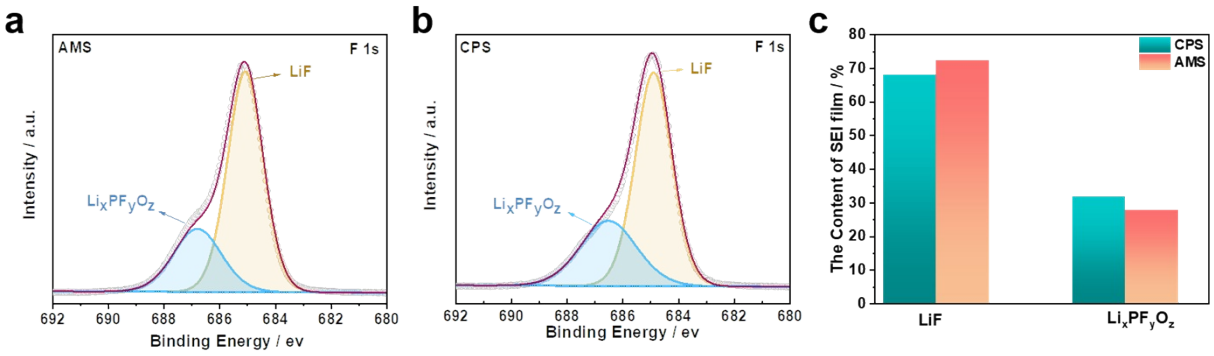

Fig. S21 F 1s XPS spectra of the lithium metal surface after long cycles of assembling lithium symmetric coin cells with AMS and CPS.

23. Charge and discharge curves of $LiFePO_4$ / AMS / Li at different rates

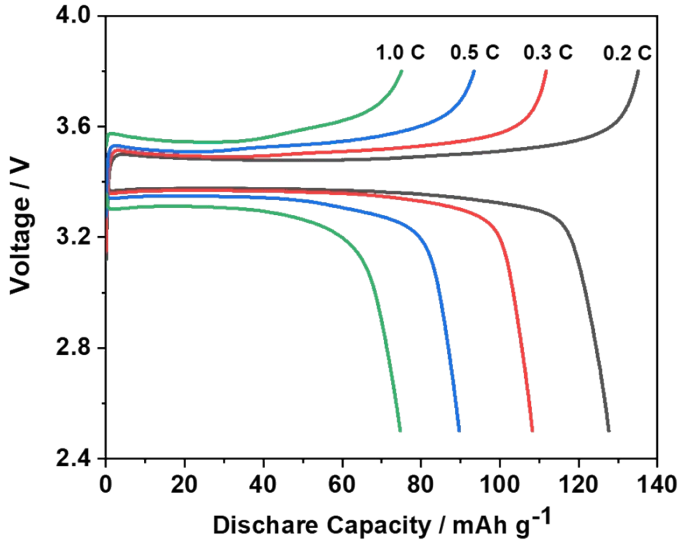

Fig. S22 Charge and discharge curves of $LiFePO_4$ / AMS / Li at different rates.

24. Comparations of the AMS with other reported separators

Table S1. Comparations of cycle time, current density, and areal capacity of the AMS developed in this work with other reported separators

Sample	Current Density ($mA \cdot cm^{-2}$)	Capacity ($mAh \cdot cm^{-2}$)	Cycle Time (h)	Ref.
AMS	**5.0**	**2.5**	**4000**	**This work**
IO-66 / PVA	0.5	0.5	400	7
B / 2D MOF-Co	2.0	1.0	400	10
HKUST-1 / PVDF-HFP	10.0	5.0	1000	11
NiCo-PBA / PAN	5.0	10.0	3000	12
Zr-MOCN@PP	10.0	10.0	450	13
GO@PP	1.0	1.0	200	14
MgF_2@PP	1.0	1.0	1600	15
F-BNNSs@PP	10.0	1.0	700	16
MoN@NG / PP	5.0	0.5	1500	17
PVDF	3.0	1.5	1000	4
SF-PVA@PP	5.0	10.0	2000	18
SNW-1 / OPBI	0.5	5.0	800	19
TPB-$BD(OH)_2$-COF / PVDF	5.0	5.0	400	20
SCOF-2@PP	1.0	1.0	350	21
PPFPA-g-Celgard	3.0	1.0	400	22

25. References

1 J. Cervera, A. Alcaraz, B. Schiedt, R. Neumann and P. Ramírez, *J. Phys. Chem. C*, 2007, **111**, 12265-12273.

2 N. Sheng, S. Chen, M. Zhang, Z. Wu, Q. Liang, P. Ji and H. Wang, *ACS Appl Mater. Interfaces*, 2021, **13**, 22416-22425.

3 C. Cheng, G. Jiang, G. P. Simon, J. Z. Liu and D. Li, Nat. Nanotechnol. 13(2018) 685-690.

4 H. Daiguji, P. Yang and A. Majumdar, *Nano Lett*., 2004, **4**, 137-142.

5 Z. Wang, W. Huang, J. Hua, Y. Wang, H. Yi, W. Zhao, Q. Zhao, H. Jia, B. Fei and F. Pan, *Small Methods*, 2020, **4**, 2000082.

6 S.-W. Lv, J.-M. Liu, C.-Y. Li, H. Ma, Z.-H. Wang and N. Zhao, S. Wang, *New J. Chem.*, 2019, **43**, 7770-7777.

7 C. Zhang, L. Shen, J. Shen, F. Liu, G. Chen, R. Tao, S. Ma, Y. Peng and Y. Lu, *Adv. Mater.*, 2019, **31**, 1808338.

8 Q. Zhao, R. Zhou, C. Wang, J. Kang, Q. Zhang, J. Liu, Y. Jin, H. Wang, Z. Zheng and L. Guo, *Adv. Funct. Mater.*, 2022, **33**, 2112711.

9 K. Chen, L. Yao and B. Su, *J. Am. Chem. Soc.*, 2019, **14**, 8608-8615.

10 Y. Li, S. Lin, D. Wang, T. Gao, J. Song, P. Zhou, Z. Xu, Z. Yang, N. Xiao and S. Guo, *Adv. Mater.*, 2020, **32**, 1906722.

11 Y. He, Z. Chang, S. Wu, Y. Qiao, S. Bai, K. Jiang, P. He and H. Zhou, *Adv. Energy Mater.*, 2018, **8**, 1802130.

12 M. Du, Z. Peng, X. Long, Z. Huang, Z. Lin, J. Yang, K. Ding, L. Chen, X. J. Hong, Y. P. Cai and Q. Zheng, *Nano Lett.*, 2022, **22**, 4861-4869.

13 L. Sheng, Q. Wang, X. Liu, H. Cui, X. Wang, Y. Xu, Z. Li, L. Wang, Z. Chen, G. L. Xu, J. Wang, Y. Tang, K. Amine, H. Xu and X. He, *Nat. Commun.*, 2022, **13**, 172.

14 D. Han, X. Wang, Y. N. Zhou, J. Zhang, Z. Liu, Z. Xiao, J. Zhou, Z. Wang, J. Zheng, Z. Jia,

B. Tian, J. Xie, Z. Liu and W. Tang, *Adv. Energy Mater.*, 2022, **12**, 2201190.

15 L. Tan, C. Wei, Y. Zhang, Y. An, S. Xiong and J. Feng, *Chem. Eng. J.*, 2022, **44**, 136243.

16 T. Ma, R. Wang, S. Jin, S. Zheng, L. Li, J. Shi, Y. Cai, J. Liang and Z. Tao, *ACS Appl Mater. Interfaces*, 2021, **13**, 391-399.

17 F. Ma, K. Srinivas, X. Zhang, Z. Zhang, Y. Wu, D. Liu, W. Zhang, Q. Wu and Y. Chen, *Adv. Funct. Mater.*, 2022, **32**, 2206113.

18 X. Li, L. Yuan, D. Liu, M. Liao, J. Chen, K. Yuan, J. Xiang, Z. Li and Y. Huang, *Adv. Funct. Mater.*, 2021, **31**, 2100537.

19 Y. Min, L. Guo, G. Wei, D. Xian, B. Zhang and L. Wang, *Chem. Eng., J.* 2022, **443**, 136480.

20 Y. Yang, S. Yao, Z. Liang, Y. Wen, Z. Liu, Y. Wu, J. Liu and M. Zhu, *ACS Energy Lett.*, 2022, **7**, 885-896.

21 J. Xu, S. An, X. Song, Y. Cao, N. Wang, X. Qiu, Y. Zhang, J. Chen, X. Duan, J. Huang, W. Li and Y. Wang, *Adv. Mater.*, 2021, **33**, 2105178.

22 S. Zheng, L. Mo, K. Chen, A. L. Chen, X. Zhang, X. Fan, F. Lai, Q. Wei, Y. E. Miao, T. Liu and Y. Yu, *Adv. Funct. Mater.*,2022, **32**, 2201430.